Direct Simulation Monte Carlo Solution of Subsonic Flow Through Micro/Nanoscale Channels

Ehsan Roohi

Masoud Darbandi[1]
e-mail: darbandi@sharif.edu

Vahid Mirjalili

Department of Aerospace Engineering,
Sharif University of Technology,
P.O. Box 11365-8639,
Tehran 11365, Iran

We use a direct simulation Monte Carlo (DSMC) method to simulate gas heating/cooling and choked subsonic flows in micro/nanoscale channels subject to either constant wall temperature or constant/variable heat flux boundary conditions. We show the effects of applying various boundary conditions on the mass flow rate and the flow parameters. We also show that it is necessary to add a buffer zone at the end of the channel if we wish to simulate more realistic conditions at the channel outlet. We also discuss why applying equilibrium-based Maxwellian distribution on molecules coming from the channel outlet, where the flow is nonequilibrium, will not disturb the DSMC solution. The current velocity, pressure, and mass flow rate results are compared with different analytical solutions of the Navier–Stokes equations. Although there are good agreements between the DSMC results and the analytical solutions in low compressible flow, the analytical solutions yield incorrect velocity and mass flow rate values in short micro/nanochannel flows with high compressibility and/or choked flow conditions. [DOI: 10.1115/1.3139105]

Keywords: DSMC, nanochannel, microchannel, subsonic flow, choked flow, heat flux boundary condition

1 Introduction

Micro- and nanochannels are widely encountered in microelectromechanical systems (MEMS). To enhance the design and performance of such systems, it is necessary to achieve a deeper understanding of their flow and heat transfer behaviors. The gas rarefaction is a main parameter to evaluate these systems provided that the Knudsen number is sufficiently large. In such conditions, the solutions are to be established based on the kinetic principles such as those in treating the Boltzmann equation. The nonequilibrium gas flow problems need the numerical treatments of the Boltzmann equation. However, the complexity of the Boltzmann equation promotes the use of alternative methods such as the direct simulation Monte Carlo (DSMC). DSMC is one of the most successful particle simulation methods and is widely used in analyzing rarefied gas flows [1].

The application of DSMC for solving the rarefied micro/nanoflows was primarily focused on high speed flows [2]. The extension of DSMC to low speed micro/nanoflow applications requires specific boundary condition considerations at the inlet/outlet sections. For example, Liou and Fang [3] used the characteristics theory to specify the back pressure condition. They simulated flow in microchannels with suitable accuracy. Wang and Li [4] provided further improvement in applying inlet boundary conditions in low speed flow treatment via considering the effect of inlet pressure on the velocity field right at the channel inlet. Using this idea, Le et al. [5] studied the flow and heat transfer behavior in microchannels with parallel and series arrangements. Chong [6] also studied the choked subsonic flow in microscales. He reported that the sonic region would appear only near the midchannel. The current workers simulated channels with different flow regimes and discussed different possible choices to simulate the choked flow in micro/nanoscale channels [7].

The objective of this work is to provide a deeper understanding of subsonic flow and heat transfer behaviors in micro/nanoscale channels. The current work provides two important contributions to micro/nanoscale flow study. First, we study the effects of gas heating or cooling on the flow behavior in subsonic regimes. Second, we elaborate the choked subsonic flow more deeply and emphasize the importance of inserting a buffer zone at the channel outlet. We compare our DSMC mass flow rate magnitude, pressure distribution, and velocity profile with different analytical derivations. We consider both mono-atomic (helium) and diatomic (nitrogen) gases and discuss the differences in their behaviors. Generally, our investigation shows that the past references have neither deeply investigated the physics of flow under various heat flux boundary conditions nor practically considered the correct treatment of outlet boundary conditions in simulating the choked subsonic flow [2–6]. These topics are properly addressed in this paper.

2 The DSMC Method

DSMC is a numerical tool to solve the Boltzmann equation based on direct statistical simulation of the molecular processes described by the kinetic theory [1]. It is considered as a particle method in which particle represents a large bulk of real gas molecules. The primary principle of DSMC is to decouple the motion and collision of particles during one time step. The implementation of DSMC needs breaking down the computational domain into a collection of grid cells. The cells are divided into subcells in each direction. The subcells are then utilized to facilitate the selection of collision pairs. After fulfilling all molecular movements, the collisions between molecules are simulated in each cell separately. In the current study, variable hard sphere collision model is used and the collision pair is chosen based on the no time counter method [1].

[1]Corresponding author.

Contributed by the Heat Transfer Division of ASME for publication in the JOURNAL OF HEAT TRANSFER. Manuscript received July 4, 2008; final manuscript received April 2, 2009; published online June 24, 2009. Review conducted by Satish G. Kandlikar. Paper presented at the Sixth International Conference on Nanochannels, Microchannels and Minichannels (ICNMM2008), Darmstadt, Germany, June 23–30, 2008.

Table 1 Details of the chosen test cases $T_{in}=300$ K

Case	1	2	3	4	5	6	7	8
Gas	He	He	He	He	He	N_2	N_2	He
h (μm)	1	1	1	1	1	0.30	0.45	1.12
$AR(L/h)$	4	4	4	4	4	6.66	4.44	4.44
Kn_{in}	0.055	0.055	0.055	0.055	0.055	0.074	0.050	0.050
λ_{im} (μm)	0.055	0.055	0.055	0.055	0.055	0.022	0.022	0.056
Kn_o	0.140	0.163	0.143	0.061	0.128	0.388	0.169	0.177
M_{in}	0.192	0.182	0.218	0.425	0.257	0.156	0.24	0.214
M_o	0.586	0.585	0.609	0.648	0.640	0.875	0.943	0.923
Buffer	No	No	No	No	No	Yes	Yes	Yes
Grid[a]	A	A	A	A	A	A+B	A+B	A+B
P_b (kPa)	108	107	107	120	109	6.73	4.91	4.83
P_e (kPa) (DSMC)	108	107	107	120	109	17.5	24.5	21.1
P_{in} (kPa)	308	314	309	358	313	99.7	98.1	97.5
Applied PR	2.851	2.934	2.881	2.983	2.870	15	20	20
Real PR	2.851	2.934	2.881	2.983	2.870	5.69	4.00	4.62
Heat condition	$T_w=300$	$T_w=350$	$q_w=0$	$q_w=-5$	Variable q_w	$T_w=323$	$T_w=300$	$T_w=300$
Re_{in} (DSMC)	5.84	5.20	5.84	10.99	6.86	5.55	6.68	7.02
Re_{in} (analytical)	6.22	5.34	6.38	12.44	7.54	5.70	7.10	7.04

[a]Grid A (100×60) is for the channel and Grid B (20×60) is for the buffer zone.

Following Wang and Li [4], we use the 1D characteristics theory to apply inlet/outlet pressure boundary conditions. The channel walls are treated as diffuse reflectors using the full thermal accommodation coefficient, see Ref. [8]. The details of boundary condition implementation can be found in Ref. [7].

3 Results and Discussion

Table 1 provides a summary of the current investigated test cases. Cases 1–5 study the effects of heat transfer on the flow field behavior in subsonic regime. Cases 6–8 study the choked subsonic flow behavior for mono-atomic and diatomic gases. We consider 10% of the wall at the channel inlet as a specular reflector. Our experience has shown that this consideration would provide more realistic conditions at the real channel inlet in micro/nanoflow treatments [9–11].

3.1 Grid Study. Figure 1 shows the geometry of channel schematically. Considering a symmetric flow, we only study one-half of the domain. The computational domain consists of two rectangles: the main channel and the buffer zone. To achieve cell independent solutions, we simulate nitrogen flow in a channel with $AR=5$, $PR=2.5$, and $Kn_{in}=0.055$ using three different grid resolutions. Figure 2(*a*) shows the pressure distributions for Grid 1 (50×30), Grid 2 (100×60), and Grid 3 (150×90) in a channel with no buffer zone. A finer grid resembles that the preceding coarse cell was divided into 2×2 subcells. The solutions are compared with the first-order analytical Navier–Stokes (NS) solution [12] and DSMC [3]. Figure 2(*b*) presents the current pressure deviations from the linear pressure distribution. It is observed that Grids 2 and 3 provide similar pressure deviations. Therefore, we continue our study using Grid 2. Our study shows that Grid 2 is also accurate for choked flow simulation because the choking PR along the channel is not that high. As seen in Table 1, the highest PR is 5.69 for Case 6.

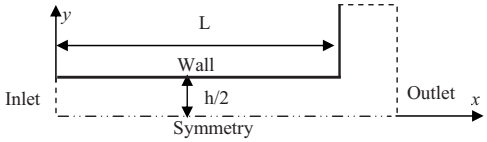

Fig. 1 Geometry of the channel and its outlet buffer

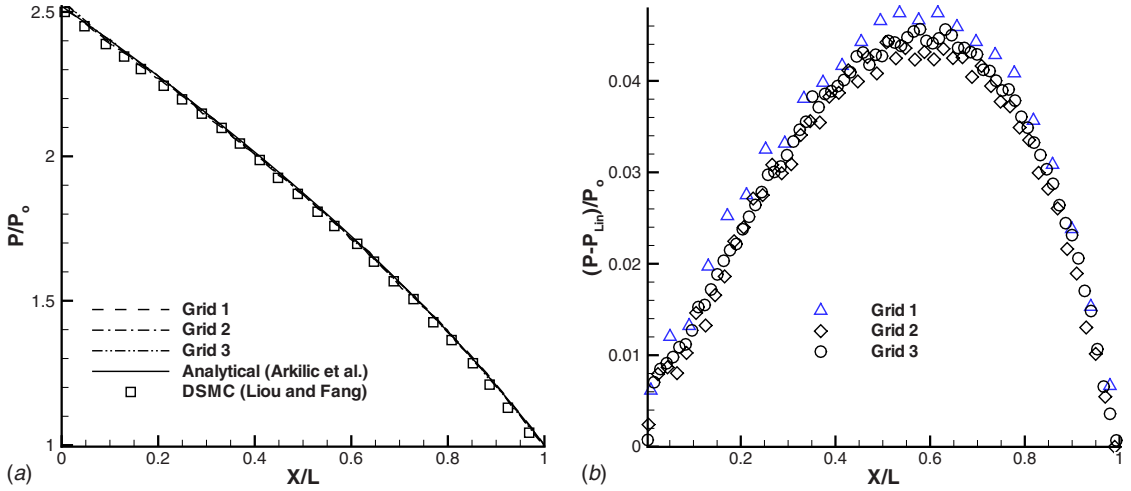

Fig. 2 Grid study and comparison with DSMC [3] and analytical NS [12] solution: (*a*) centerline pressure distribution and (*b*) centerline pressure deviation

Table 2 Comparative study of mass flow rates ($Q\times10^5$)

Current	DSMC [13]	Numerical NS [13]	Analytic NS [12]
2.18	2.17	2.16	2.17

3.2 DSMC Validation. We set 20–25 molecules in each cell at time zero. Since the gas temperature is relatively low for the chosen cases, the vibrational energy is not taken into account for the diatomic nitrogen molecules [1]. The values of mass flow rate at the inlet and outlet were monitored until achieving negligible differences between two consequent time steps. After that, we continued the computations to suppress the inherent DSMC statistical fluctuations. To validate the current mass flow rate, we observe that the past experiments in microchannels have mostly focused on long channels having low speed isothermal flows. Since our study is limited to relatively short channels, we compare our results with the DSMC and numerical NS solutions of Cai et al. [13] and the analytical NS solution of Arkilic et al. [12]. Table 2 provides the details of comparisons for a gas (oxygen) flow in a channel with $PR=2.5$ and $AR=28.30$. As seen in this table, there are good agreements among them.

3.3 Subsonic Flow With Heat Transfer, Cases 1–5. In this section, we study subsonic helium flow in a channel subject to constant wall temperature and constant/variable wall heat flux boundary conditions. Our literature survey shows that the past investigations have mostly focused on constant wall temperature study [5,14].

3.3.1 Wall Thermal Boundary Condition Study. The details of Cases 1–5 are provided in Table 1. The table also provides the DSMC and the analytical Reynolds number magnitudes defined as $\mathrm{Re}_{\mathrm{in}}=\rho uh/\mu=Q/\mu$ and $\mathrm{Re}_{\mathrm{in}}=\sqrt{\gamma\pi/2}\mathrm{M}_{\mathrm{in}}/\mathrm{Kn}_{\mathrm{in}}$, respectively. As seen, there are close agreements between the DSMC prediction and the analytical solution.

Figure 3 shows the distributions of wall heat flux per unit width (positive from the wall to the fluid) for Cases 2 and 5. For Case 2, the heat flux is calculated from

$$q_w=\frac{\sum\varepsilon^i-\sum\varepsilon^r}{A\Delta t} \tag{1}$$

where $\Sigma\varepsilon$ is the sum of the averaged molecular energies, A is the area, Δt is the interaction time, and i and r stand for the incidence and reflected molecules, respectively. Figure 3 shows that the gas is heated in Case 2 because the wall temperature is higher than

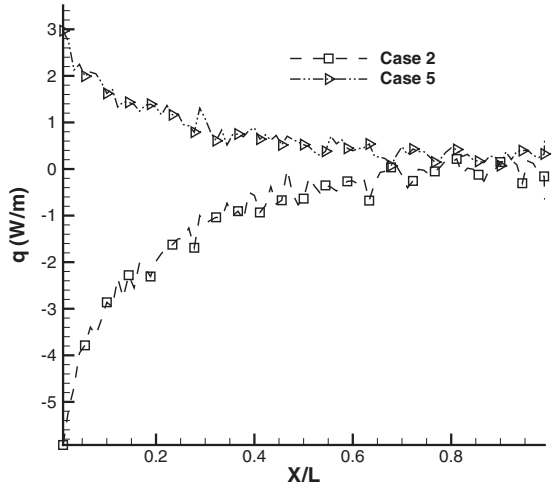

Fig. 3 Current DSMC wall heat flux distributions

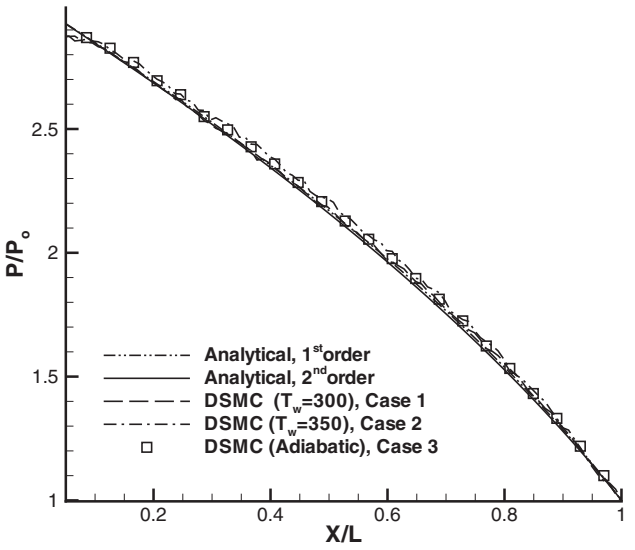

Fig. 4 Pressure distributions and comparison with the first-[12] and second-order [16] NS analytical solutions

that of the main flow. The rate of heat transfer decreases in the downstream of the channel and it almost vanishes near the exit.

In Cases 3–5, we examine the specified heat flux (SHF) boundary condition at the wall, as suggested by Wang et al. [15]. They developed an inverse temperature sampling technique, which benefits from calculating the wall temperature from the SHF at the wall. To simulate SHF in DSMC, we use

$$\bar{\varepsilon}_j^r=\bar{\varepsilon}_j^i-\Delta\bar{\varepsilon}=\bar{\varepsilon}_{\mathrm{tr}}+\bar{\varepsilon}_{\mathrm{rot}}=2kT_j+\frac{\xi_{\mathrm{rot}}kT_j}{2} \tag{2}$$

where $\Delta\bar{\varepsilon}=q_w/(\alpha AN_{\mathrm{imp}}\Delta t)$ is the average energy transferred to the wall, ξ_{rot} is the number of rotational degrees of freedom, and N_{imp} is the number of molecules impinging the surface. Hence, the wall temperature is calculated from

$$T_j=\frac{\varepsilon_j^i-\Delta\bar{\varepsilon}}{k(2+\xi_{\mathrm{rot}}/2)} \tag{3}$$

We use Eq. (3) to find the temperature at the surface. Cases 4 and 5 are modeled using variable $\Delta\bar{\varepsilon}$ distributions. In Case 3 with $\Delta\bar{\varepsilon}=0$, the total energy of incident molecules would be carried out by the reflected molecules.

3.3.2 Results and Discussion. Figure 4 shows the centerline pressure distributions for Cases 1–3 and compares them with the first-[12] and second-order [16] NS analytical solutions. Good agreement is observed between Cases 1 and 3, while Case 2 shows slight deviations from them. This can be attributed to gas heating status, which causes more serious density variation and compressibility effect. As is known, the compressibility makes the pressure distribution more nonlinear. Indeed, the analytical pressure distributions are derived assuming low Reynolds number ($\mathrm{Re}<O(1)$) isothermal flow in long microchannels, where the ratio of inertial terms (I) to diffusion terms (D), i.e., $I/D\approx\mathrm{Re}(h/L)\Delta P/P_{\mathrm{in}}$, is negligible. However, the current channel aspect ratio is small and the Reynolds number is $O(10)$. Therefore, the inertial to diffusion ratio is not negligible. This justifies the difference between the DSMC and the analytical solutions, specifically for Case 2, with gas flow heating condition.

Figure 5 shows the distributions of centerline and wall temperatures and centerline Mach number for Cases 1–5. If the wall temperature is equal to the inlet flow temperature, i.e., Case 1, gas heating becomes negligible in most of the channel length. Therefore, we expect to observe close agreement between Cases 1 and

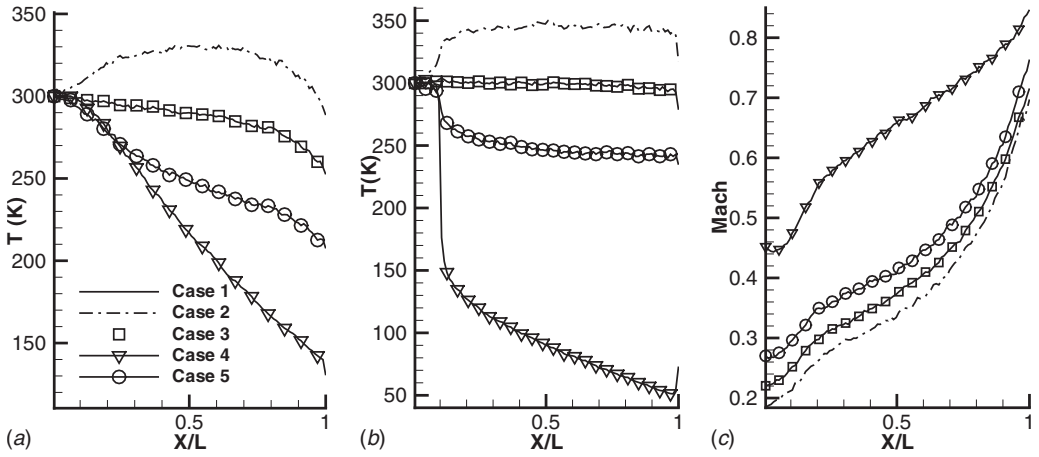

Fig. 5 Temperature and Mach number distributions, Cases 1–5: (*a*) centerline temperature, (*b*) near wall temperature, and (*c*) centerline Mach

3. For a higher wall temperature, i.e., Case 2, the centerline temperature increases initially, reaches to a maximum of 330 K around $X/L=0.6$, and starts decaying as soon as the wall heat flux vanishes (see Fig. 3). The expansion at the channel outlet reduces the temperature more rapidly. Meanwhile, the flow temperature adjacent to the wall increases to a value close to the wall temperature. The temperature distribution behaves differently for Case 1. The centerline temperature remains constant and equal to the inlet temperature up to the expansion near the outlet, where a rapid decrease occurs. The heat flux distribution applied to Case 5 causes a wall temperature drop from 300 K to 250 K along the channel. The behavior of temperature field in Case 4 shows a semilinear decrease in centerline temperature. Alternatively, its wall temperature rapidly drops from the inlet temperature to 150 K, followed by a semilinear decrease until reaching the channel exit. Vakilipour and Darbandi [10] simulated low-speed flow in microchannels using SHF boundary conditions. Their simulations showed linear increase in either wall or centerline temperatures under positive wall heat flux condition. Contrary to the simulations in Ref. [10], all the simulated cases are compressible in this study. Since the flow speed near the wall is relatively low, we observe a linear decrease in wall temperature due to a negative heat flux. The centerline temperature performs slight nonlinearity, which is due to the effects of compressibility at the midchannel.

Figure 5(*c*) shows the centerline Mach number in the channel. The maximum M_{in} belongs to Case 4 and the minimum to Case 2. Considering a fixed inlet temperature for all cases, it is concluded that gas cooling increases the velocity and mass flow rate. Figure 6 shows the Mach number and temperature maps for Case 4. The variation in the Mach number is finite in this condition. The temperature map shows a rapid decrease in temperature until the midchannel, while the reduction in the temperature is less pronounced in the second half.

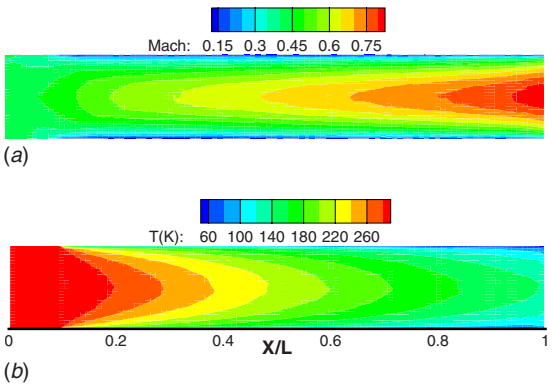

Fig. 6 Mach number and temperature maps, Case 4

3.3.3 Mass Flow Rate Study. Arkilic et al. [17], Graur et al. [18], and Karniadakis et al. [16] derived analytical solutions to predict the mass flow rate in microchannels as follows:

$$Q_{\mathrm{Ark}} = S_1[(PR^2-1)+12\ \mathrm{Kn}_o(PR-1)] \tag{4}$$

$$Q_{\mathrm{Gra}} = S_1[PR^2-1+12\ \mathrm{Kn}_o(PR-1)+S_2\ \ln(PR)] \tag{5}$$

$$Q_{\mathrm{Kar}} = S_3[(PR+1)+12\ \mathrm{Kn}_o+S_4\ \ln(S_5)] \tag{6}$$

where $S_1=h^3P_0^2/(24\mu RTL)$, $S_2=24\ \mathrm{Kn}_o^2/k_\lambda^2$, $S_3=h^3P_0(P_i-P_0)/(24\mu RTL)$, $S_4=12\ \mathrm{Kn}_o^2\ b/(PR-1)$, $S_5=(PR-b\ \mathrm{Kn}_o)/(1-b\ \mathrm{Kn}_o)$, $k_\lambda=1.02$, $b=-1$, μ is the viscosity coefficient, and R is the gas constant. The derivations of Eqs. (4)–(6) are subject to assumptions such as isothermal-low Mach number flow and long channel with locally fully developed condition. Table 3 presents the DSMC mass flow rates for Cases 1 and 2 and compares them with the analytical solutions. Evidently, the analytical solutions are not applicable to other simulated cases such as Cases 4 and 5, which are not isothermal. There are good agreements between the current DSMC results and Eqs. (4) and (6). Equation (5) predicts higher mass flow rate than the two other expressions. The analytical NS solutions given by Eqs. (4)–(6) confirm that the increase in flow temperature reduces the mass flow rate because the temperature appears in the denominator. The equation of state indicates that the increase in temperature for a given pressure ratio leads to a reduction in density. Therefore, it is expected that the mass flow rate decreases as the inlet temperature increases.

3.4 Choked Subsonic Flow. In this section, we study the choked subsonic flow and evaluate the effect of specifying back pressure at the real outlet and at the outer region of a buffer zone.

3.4.1 Role of Buffer Zone on the DSMC Solution. Back to Fig. 1, the chosen buffer zone sizes are $0.2L$ and $1.33h$. It is important to note that the use of buffer zone is to capture the choked condition at the channel exit precisely. Figure 7 shows the Mach

Table 3 DSMC and analytical mass flow rates ($Q\times10^5$)

Cases	DSMC	Eq. (4)	Eq. (5)	Eq. (6)
1	10.76	10.71	11.20	10.47
2	9.70	10.02	10.06	9.75

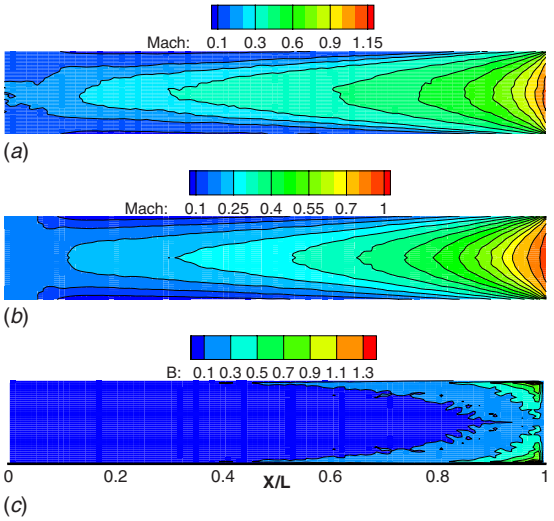

Fig. 7 Displaying results for Case 6 including: (*a*) Mach number in the channel without buffer zone, (*b*) Mach number in the channel with buffer zone, and (*c*) the parameter *B* in the channel with buffer zone

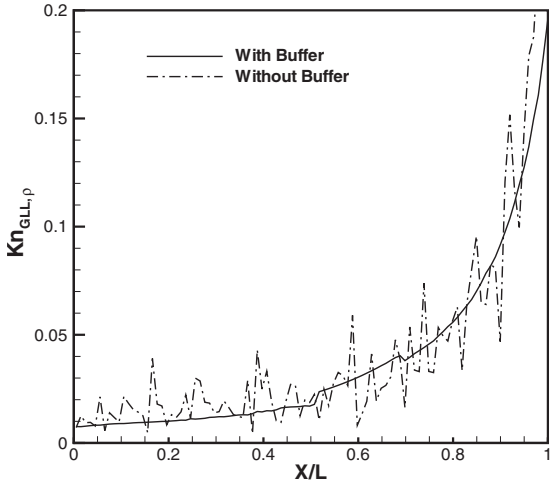

Fig. 8 Knudsen number based on GLL of density, Case 7

number maps for Case 6. Enforcing a back pressure, i.e., $P_b = 6.73$ kPa, much lower than the choking pressure, i.e., $P_e = 17.5$ kPa, at the real channel outlet, it leads to incorrect velocity or Mach number estimations at the outlet. In fact, it predicts a nonphysical supersonic flow with $M_e = 1.15$. If the pressure is specified right at the real channel outlet, two types of error appear in the solution. First, due to applying the back pressure via characteristics theory [4], the exit pressure directly influences the velocity of the molecules adjacent to the outlet boundary and the thermodynamic properties of the cells located near the outlet. Once choking occurs, the exit pressure does not drop anymore and consequently, applying a back pressure less than the choking pressure right at the channel outlet results in a nonphysical prediction of the flow field. Second, from the molecular gas dynamics point of view, we consider a Maxwellian distribution for velocity and number density of molecules that enter from the inlet and outlet boundaries to the solution domain. As the exit Mach number increases, the gradient of flow parameters increases at the channel outlet; hence, the flow parameter distributions may not exactly follow the Maxwellian distribution. There are different equilibrium breakdown parameters. One is local Knudsen number based on the gradients local length (GLL) of properties and is defined as $\mathrm{Kn}_{\mathrm{GLL},\phi} = (\lambda/\phi)|d\phi/dl|$, where ϕ is an arbitarary flow parameter and $\mathrm{Kn}_{\mathrm{GLL}} = \max(\mathrm{Kn}_{\mathrm{GLL},\rho}\ \mathrm{Kn}_{\mathrm{GLL},V}, \mathrm{Kn}_{\mathrm{GLL},T})$. The other one is the *B* parameter, which is considered as the maximum value of the shear stress and heat flux magnitudes, i.e., $B = \max(|q_i^*|, |\tau_{ij}^*|)$, where $q_i^* = -(\kappa/P)(2m/kT)^{0.5}\nabla T$ and $\tau_{ij}^* = (\mu/P)(V_{i,j} + V_{j,i} - 2/3 V_{k,k}\delta_{ij})$. Indeed, the equilibrium breakdown occurs when $\mathrm{Kn}_{\mathrm{GLL}} > 0.05$ [19]. Garcia and Aldert [20] indicated that the validity of Chapman–Enskog distribution fails if $B = 0.1$. Figure 7(*c*) shows contours of *B* in the channel. Although the variation in this parameter is small up to $X/L = 0.45$, it starts exceeding 0.1 near the wall from this point. In general, the equilibrium breakdown is due to sharp property gradients and rarefaction. We observe both of these, i.e., high flow parameter gradients and low density near the wall close to the channel outlet. It is concluded that the subsonic choked flow is highly nonequilibrium especially near the outlet region.

To study the role of the buffer zone on the solution, we compute $\mathrm{Kn}_{\mathrm{GLL},\rho}$ in the channel with and without buffer zones for Case 7. As shown in Fig. 8, $\mathrm{Kn}_{\mathrm{GLL},\rho}$ shows nonoscillatory variations for the case with a buffer zone. Meanwhile, the case without buffer zone shows a wavy behavior. $\mathrm{Kn}_{\mathrm{GLL},\rho}$ exceeds the limiting value of 0.05 as it approaches the channel outlet. Our study shows that the number of incoming molecules from the outlet is relatively low in comparison with the actual number of molecules in the domain. Therefore, using Maxwellian distribution for the incoming molecules at the channel outlet does not considerably disturb the solution. In fact, the characteristic-based implementation of back pressure right at the outlet enforces a very low back pressure there, which is nonphysical. Consequently, the magnitudes of velocity, temperature, and density of the cells adjacent to the outlet become incorrect. To implement the physics of flow properly, we apply the back pressure right at the outer region of the buffer zone. Therefore, the solution is permitted to be adjusted freely at the real outlet. This can help to obtain a reasonable Mach number ($M = 1$) at the outlet.

In order to evaluate our choked flow solution, we use an analytical solution to calculate the outlet pressure for nonisothermal flows [21] as follows:

$$\ln\left(\frac{P_o}{P_1}\right) = -\ln\left(\frac{\overline{M}_o}{M_1}\right)[1 + \chi(M_1)] \tag{7}$$

where $\chi(M_1) = \ln(J_o/J_1)/[\ln(\overline{M}_o^2/M_1^2)]$, $J_1 = (1 + (\gamma - 1)\omega M_1^2/2)$, and $\omega = (\int_A u^3 dA)/(A\bar{u}^3)$. Table 4 compares our DSMC exit pressure with the one derived from Eq. (7) for Cases 6–8. As seen, the analytical calculations predict the choked exit pressure suitably.

3.4.2 Temperature and Mach Number Distributions. Figure 9 shows the centerline temperature and Mach number distributions for Cases 6–8. For Case 6, there is an increase in the first half of the channel followed by a gas cooling in the second half. This is due to strong expansion occurring at the channel outlet. Figure 9(*a*) shows that helium (Case 8) experiences more cooling and rarefaction than nitrogen (Case 7) for the same $\mathrm{Kn}_{\mathrm{in}}$ and *PR*. Figure 9(*b*) shows that the helium Mach number is lower than that of nitrogen along the channel. Consistent with the results shown in Fig. 5(*c*), a hotter condition results in a lower Mach number along the channel.

Figure 10 shows temperature profiles at six axial sections for Case 7. It is observed that the temperature field behaves in a

Table 4 DSMC and analytical [21] choked pressures

Case	DSMC	Eq. (7)
6	17.50	16.05
7	24.50	23.10
8	21.10	20.48

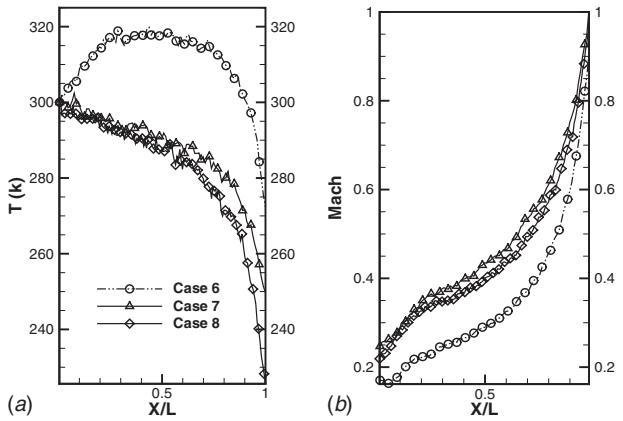

Fig. 9 Centerline temperature and Mach number distributions

complicated manner due to the mixed effects of rarefaction, wall heat transfer, thermal boundary layer development, and rapid conversion of the internal energy to a kinetic one. There is a slight heat transfer between the wall and its adjacent gas molecules close to the inlet section; therefore, we observe small temperature increase near the wall. This is followed by temperature decrease due to flow acceleration. Since the acceleration is more pronounced at the channel centerline, the temperature reduces there more rapidly. The figure shows different characteristics of mean flow and thermal boundary layer. It is observed that the thermal layer has influenced into most of the channel height at $X/L=0.6$.

3.4.3 Mass Flow Rate. Table 5 presents the DSMC mass flow rates for Cases 6–8 and compares them with the analytical solutions, i.e., Eqs. (4)–(6). We considered a choking pressure ratio along the channel instead of a real pressure ratio to calculate the analytical mass flow rates. It is observed that the analytical solutions fully underestimate the real mass flow rate in choked flow conditions. This point is expected because the underlying assumptions on which these solutions are derived are invalid here. A locally fully developed flow condition states that the pressure and density are uniform in any cross section, and the convection term is much smaller than the diffusion term in the momentum equation. As shown in Fig. 9, there are large gradients in the Mach number and temperature near the channel outlet. It was already

Table 5 DSMC and analytical mass flow rates ($Q\times10^5$)

Case	DSMC	Eq. (4)	Eq. (5)	Eq. (6)
6	9.20	0.62	0.69	0.75
7	11.00	1.62	1.69	1.84
8	13.10	1.27	1.33	1.43

shown that the rarefied flow permits more mass flow rate than the continuum one [12,17]. The current results are in contrast with the results reported by Chong [6]. His DSMC simulation showed lower mass flow rates than the NS analytical solutions [17]. Chong employed the applied pressure ratios along the channel in Eq. (4). However, we show that the applied pressure ratio may not be achieved in real physics because the channel pressure ratio does not drop anymore once the flow is choked in the channel, see Table 1.

3.4.4 Velocity Distribution. Figure 11 shows the normalized velocity profiles of the DSMC and analytical solutions of Karniadakis et al. [16] at three different axial locations for Case 8. We use the average velocity from DSMC and analytical solutions to normalize each velocity profile. Figure 11 shows that the maximum normalized velocity for the DSMC is always lower than that of the analytical solution. As shown in Table 6, this is due to a higher average velocity of the DSMC simulations and its usage to normalize the DSMC velocity profile. The mean velocities in Table 6 show that the average velocity in simulation is approximately 37–40% more than the analytical predictions at the chosen locations. This difference can be attributed to a greater pressure gradient under choked condition. As seen in Fig. 11, the slip velocities are higher than those of the analytical predictions. This was similarly observed for Cases 6 and 7.

3.5 DSMC Versus the Analytical Solutions. Up to here, we presented a few analytical solutions to show how accurate they are if they are used to calculate subsonic micro/nanochannel flows. As is known, the rarefaction and compressibility cause the microfluid behaviors to be different from those in macroscale study. The analytical solutions provided in this work are for standard hydrodynamic flows. There are many rarefaction effects which cannot be reproduced in classical hydrodynamics, including bimodal temperature profiles, nonconstant pressure profiles across the channel, and many more, see Ref. [22]. Alternatively, the higher-order

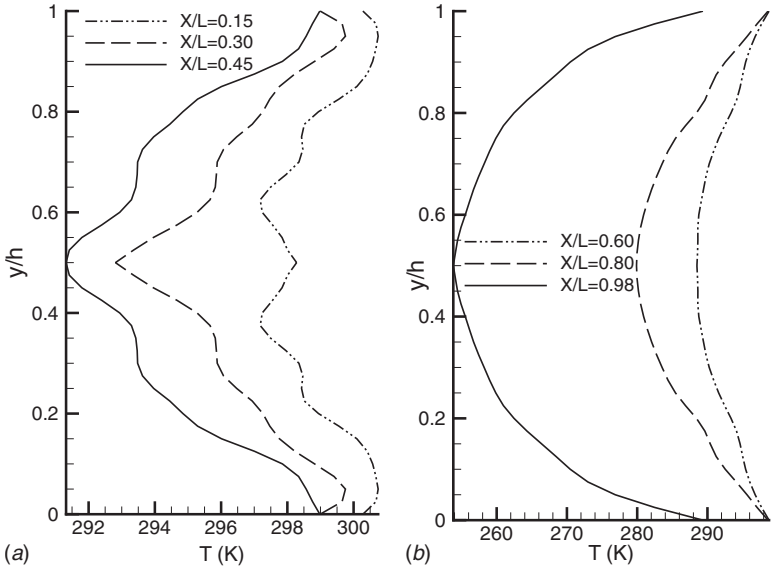

Fig. 10 Temperature profiles at different axial sections, Case 7

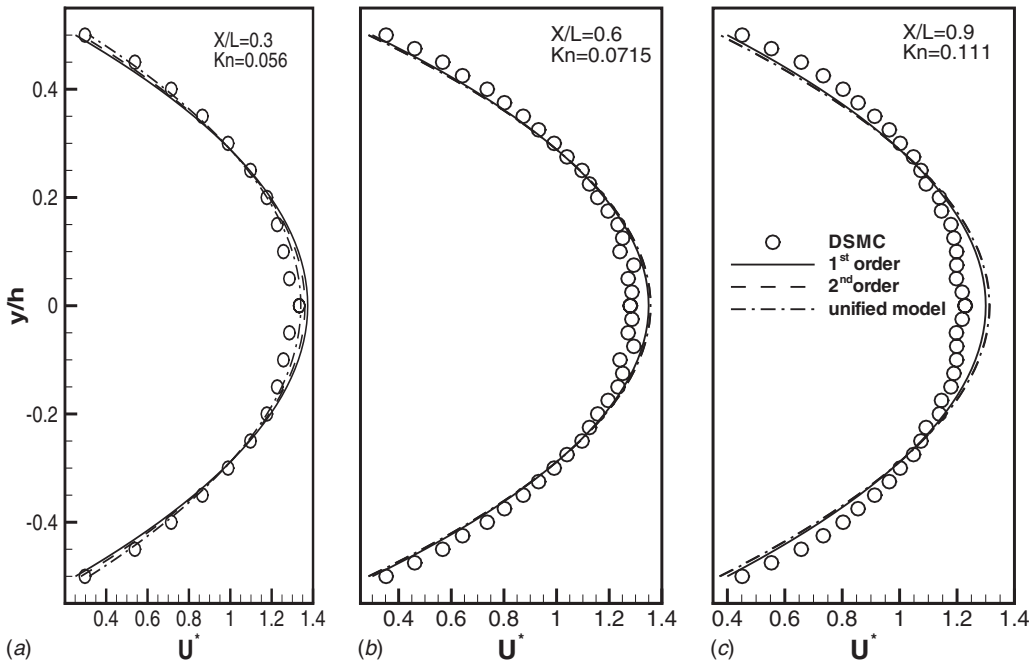

Fig. 11 Normalized velocity profiles of DSMC and analytical solutions [16], Case 8

Table 6 DSMC and the second-order analytical [16] mean velocities

X/L	0.3	0.6	0.9
$\bar{U}_{\text{analytical}}$ [16]	69.70	98.46	147.40
$\bar{U}_{\text{DSMC}}$	90.90	125.40	205.70
$\bar{U}_{\text{DSMC}}/\bar{U}_{\text{analytical}}$	1.41	1.37	1.39

continuum-based equations, such as the regularized 13 (R13) moment [23,24], were extended to reveal more unique aspects of microflows. Meanwhile, most of these latter equations are subject to some restrictions such as stability, difficulty in finding appropriate boundary conditions, and limitation to mono-atomic gases [23]. To benefit from both continuum-based equations and DSMC, the current authors are willing to extend their NS solver [25,26] to higher-order continuum equations and develop a hybrid continuum-DSMC solver.

4 Conclusion

We used DSMC to simulate subsonic flow with and without choking in micro/nanoscale channels subject to different thermal wall boundary conditions. It was observed that gas heating would increase the compressibility effects in the channel and would augment the nonlinearity in axial pressure distribution. For a specified pressure ratio along the channel, gas cooling causes an increase in mass flow rate. Alternatively, a negative heat flux wall boundary condition yields a linear decrease in centerline and wall temperatures in low compressible flows. To derive more realistic solutions in the case of the choked flow, it was suggested to implement the back pressure at the outer region of a buffer zone. Applying a nonphysical pressure just at the channel exit would result in incorrect velocity predictions for the molecules adjacent to the channel exit and incorrect thermodynamic properties of the cells located there. This consequently would lead to a wrong Mach number prediction at the exit. The DSMC mass flow rate and velocity profile were compared with the analytical Navier–Stokes solutions. It was concluded that the rarefaction and high compressibility of the choked flow would deteriorate the analytical predictions in short channels.

Nomenclature

AR = aspect ratio (L/h)
h = channel height (m)
k = Boltzmann constant (N m/K)
Kn = Knudsen number (Kn=λ/h)
L = channel length (m)
M = Mach number
P = pressure (Pa)
PR = pressure ratio
Q = mass flow rate per length (kg/ms)
T = temperature (K)
V = velocity (m/s)

Greek Symbols

α = thermal accommodation coefficient
κ = thermal conductivity (W/m K)
γ = specific heat ratio
λ = mean free path (m)
ρ = density (kg/m^3)
τ = shear stress (kg/m s^2)

Subscripts, Superscripts, and Accents

E = exit
in = inlet
i,j = cell indices in x and y directions
o = outlet
tr = translational energy
w = wall
$-$ = averaged

References

[1] Bird, G. A., 1994, *Molecular Gas Dynamics and the Direct Simulation of Gas Flows*, Clarendon, Oxford.
[2] Oh, C. K., Oran, E. S., and Sinkovits, R. S., 1997, "Computations of High-Speed, High Knudsen Number Microchannel Flows," J. Thermophys. Heat Transfer, **11**(4), pp. 497–505.
[3] Liou, W. W., and Fang, Y. C., 2000, "Implicit Boundary Conditions for Direct

Simulation Monte Carlo Method in MEMS Flow Predictions," Comput. Model. Eng. Sci., **1**, pp. 119–128.
[4] Wang, M., and Li, Z., 2004, "Simulations for Gas Flows in Microgeometries Using the Direct Simulation Monte Carlo Method," Int. J. Heat Fluid Flow, **25**, pp. 975–985.
[5] Le, M., Hassan, I., and Esmail, N., 2006, "DSMC Simulation of Subsonic Flows in Parallel and Series Microchannels," ASME J. Fluids Eng., **128**, pp. 1153–1163.
[6] Chong, X., 2006, "Subsonic Choked Flow in Microchannel," Phys. Fluids, **18**, p. 127104.
[7] Roohi, E., Darbandi, M., and Mirjalili, V., 2008, "DSMC Solution of Supersonic Scale to Choked Subsonic Flow in Micro to Nano Channels," ASME ICNMM 2008-62282, Germany, Jun. 23–25.
[8] Hong, C., and Asako, Y., 2008, "Heat Transfer Characteristics of Gaseous Flows in Microchannel With Negative Heat Flux," Heat Transfer Eng., **29**(9), pp. 805–815.
[9] Darbandi, M., and Vakilipour, S., 2007, "Developing Consistent Inlet Boundary Conditions to Study the Entrance Zone in Microchannels," J. Thermophys. Heat Transfer, **21**(3), pp. 596–607.
[10] Vakilipour, S., and Darbandi, M., 2009, "Advancement in Numerical Study of Gas Flow and Heat Transfer in Microchannels," J. Thermophys. Heat Transfer, **23**(1), pp. 205–208.
[11] Darbandi, M., and Vakilipour, S., 2009, "Solution of Thermally Developing Zone in Short Micro/Nano Scale Channels," ASME J. Heat Transfer, **131**(4), p. 044501.
[12] Arkilic, E. B., Schmidt, M. A., and Breuer, K. S., 1997, "Gaseous Slip Flow in Long Microchannel," J. Microelectromech. Syst., **6**, pp. 167–178.
[13] Cai, C., Boyd, I. D., Fan, J., and Candler, G. V., 2000, "Direct Simulation Methods for Low-Speed Microchannel Flows," J. Thermophys. Heat Transfer, **14**(3), pp. 368–378.
[14] Hadjiconstantinou, N. G., and Simek, O., 2002, "Constant-Wall-Temperature Nusselt Number in Micro and Nano-Channels," ASME J. Heat Transfer, **124**, pp. 356–364.
[15] Wang, Q. W., Yan, X., and He, Q., 2008, "Heat-Flux-Specified Boundary Treatment for Gas Flow and Heat Transfer in Microchannel Using Direct Simulation Monte Carlo Method," Int. J. Numer. Methods Eng., **74**, pp. 1109–1127.
[16] Karniadakis, G. E., Beskok, A., and Aluru, N., 2005, *Micro Flows and Nano Flows: Fundamentals and Simulation*, Springer-Verlag, New York.
[17] Arkilic, E. B., Breuer, K. S., and Schmidt, M. A., 2001, "Mass Flow and Tangential Momentum Accommodation in Silicon Micromachined Channels," J. Fluid Mech., **437**, pp. 29–43.
[18] Graur, I. A., Meolans, J. G., and Zeitoun, D. E., 2006, "Analytical and Numerical Description for Isothermal Gas Flows in Microchannels," Microfluid. Nanofluid., **2**, pp. 64–77.
[19] Lofthouse, A., Boyd, I., and Wright, M., 2007, "Effects of Continuum Breakdown on Hypersonic Aerothermodynamics," Phys. Fluids, **19**, p. 027105.
[20] Garcia, A., and Aldert, B., 1998, "Generation of the Chapman-Enskog Distribution," J. Comput. Phys., **140**, pp. 66–70.
[21] Harley, J., Huang, Y., Bau, H., and Zemel, J., 1995, "Gas Flow in Microchannels," J. Fluid Mech., **284**, pp. 257–274.
[22] Uribe, F. J., and Garcia, A. L., 1999, "Burnett Description for Plane Poiseuille Flow," Phys. Rev. E, **60**(4), pp. 4063–4078.
[23] Struchtrup, H., and Torrilhon, M., 2008, "Higher-Order Effects in Rarefied Channel Flows," Phys. Rev. E, **78**, p. 046301.
[24] Torrilhon, M., and Struchtrup, H., 2009, "Modeling Micro Mass and Heat Transfer for Gases Using Extended Continuum Equations," ASME J. Heat Transfer, **131**(3), p. 033103.
[25] Darbandi, M., and Schneider, G. E., 2000, "Performance of an Analogy-Based All-Speed Procedure Without Any Explicit Damping," Comput. Mech., **26**(5), pp. 459–469.
[26] Darbandi, M., Roohi, E., and Mokarizadeh, V., 2008, "Conceptual Linearization of Euler Governing Equations to Solve High Speed Compressible Flow Using a Pressure-Based Method," Numer. Methods Partial Differ. Equ., **24**(2), pp. 583–604.